

PHYSICAL REVIEW B

CONDENSED MATTER

THIRD SERIES, VOLUME 35, NUMBER 12

15 APRIL 1987-II

Observation of driven surface-plasmon modes in metal particulates above tunnel junctions

M. J. Bloemer, J. G. Mantovani, J. P. Goudonnet, D. R. James, R. J. Warmack, and T. L. Ferrell

Health and Safety Research Division, Oak Ridge National Laboratory, Oak Ridge, Tennessee 37831

(Received 20 October 1986)

Evidence is presented showing that the radiative decay of localized surface-plasmon modes from metal particulates on aluminum-alumina-gold tunnel junctions is due to these modes being driven off resonance by the fields of the gold electrode. The metal particulates are formed on top of an insulating spacer set above the gold electrode by deposition of a silver-island film.

I. INTRODUCTION

Light emission from metal-oxide-metal tunnel junctions incorporating metal particulates has been reported by a number of investigators.¹⁻⁴ The tunnel junction geometry of Ref. 1 is dissimilar to Refs. 2-4 in two respects. In Refs. 2-4, metal smokes of silver or gold were deposited directly on the oxide and subsequently buried under a noble metal, or top, electrode. In Ref. 1, metal particulates are situated above the tunnel junction by means of a MgF₂ spacer. Secondly, metal smokes are often modeled as spheres, while the particulates of Ref. 1 are better modeled as spheroids.

A theoretical model appropriate for microstructures placed on the oxide was developed in a series of papers.⁵⁻⁷ In this model, surface plasmons localized in the microstructures are excited by a fluctuating current produced by the electrons tunneling directly into the microstructures. The currents induced in these miniature antennae radiate the observed light. In the experiment by McCarthy and Lambe,¹ metal spheroids situated above the tunnel junction were pictured as coupling nonlocal surface plasmons to the photon field via surface plasmon decay. For the McCarthy and Lambe geometry, the electrons tunnel to the planar electrode. Direct tunneling to the particulates is negligible. That is, surface plasmons in the noble-metal electrode couple to surface plasmons in the particulates, and the spectrum of emitted photons depends upon the thin-film surface plasmons as well as the radiating particulates.

Recent articles⁸⁻¹¹ on surface plasmon modes in metal island films have provided the impetus for further investigations of tunnel junctions utilizing the geometry of McCarthy and Lambe. These papers present experimental and theoretical results on the excitation and radiative decay of surface plasmons in thin annealed films. Modeling

the islands as oblate spheroids was shown to yield good agreement between theory and experiment.

Light emission from metal oblate spheroids above tunnel junctions may be modeled as the last in a series of stages of energy transfer. At each stage losses are introduced which account for the low efficiency of these light-emitting devices. In a planar junction, tunneling electrons excite nonlocal, thin-film, surface-plasmon modes in the top electrode. The fields associated with these modes decay exponentially with distance from the electrode. If metal islands are in the vicinity of this interface, localized modes may be stimulated. Radiative decay of surface plasmon modes in the islands is the final step of the emission process. Thus, in this model the particulates of the island film are driven off resonance by the thin-film, surface-plasmon field induced by tunneling electrons.

In the experiment detailed below, the tunnel junction geometry used by McCarthy and Lambe is employed to present evidence for light emission due to radiative decay of localized plasmon modes driven off resonance by fields associated with the upper electrode. A straightforward calculation is given which predicts the peak position of the emission spectra. However, the calculation neglects retardation effects for large particulates and for the size of particulates used in the experiment. Retardation effects in silver particulates can have measurable effects for particulates with dimensions on the order of or greater than 40 nm. If one uses Mie theory for spherical particulates, the shift in the silver dipole surface plasmon has been found by us to be small. The main effects are the enhancement of the quadrupole mode and the subsequent effects on the radiation pattern. Nonetheless, with the light emission being primarily determined by the driving frequency, the nonretarded calculation does yield a reasonable spectrum due to the large slope of the real part of the dielectric function of silver in the visible range

(which implies a small shift in the spectrum for a large change in the eigenvalue of the real part of the dielectric function).

II. THEORY

We describe below a simple calculation of the power radiated from an oblate spheroidal metal particulate located on an insulator layer above a tunnel junction. We treat the tunneling electron as a classical particle¹² which traverses a straight line path through an oxide layer from the bottom electrode to the top electrode. For analyzing the reaction of the spheroids, we also take the trajectory to lie along a line which coincides with a surface normal that passes through the center of the metal spheroid. The origin of the coordinate system is taken to be at the center of the metal particulate.

The Fourier component of the nonretarded potential due to an electron that is normally incident upon a thin foil having a complex dielectric response function $\epsilon_F(\omega)$ and thickness L is sought on the side opposite the electron. Applying the boundary conditions at the two surfaces of the thin foil to solutions of Poisson's equation, the Fourier component of the potential is found to be

$$\Phi(R, z, \omega) = \frac{q}{v} \epsilon_F(\omega) e^{-i(\omega/v)[z_0 + (L/2) + z']} \times \int_0^\infty dk \frac{J_0(kR)}{k + i(\omega/v)} T(k, \omega) e^{-k[z + z_0 - (L/2)]}, \quad (1)$$

where $J_0(kR)$ is the zero-order Bessel function, and

$$T(k, \omega) = \left[\epsilon_F(\omega) + \tanh \left[\frac{kL}{2} \right] \right]^{-1} - \left[\epsilon_F(\omega) + \coth \left[\frac{kL}{2} \right] \right]^{-1}. \quad (2)$$

In Eq. (1), the electron with charge q travels at constant velocity from $-\infty$ to $z = z_0 - L/2$. The velocity v corresponds to that of an electron with kinetic energy equal to $|qV|$, where V is the dc bias voltage applied to the junction. The plane of the foil is the x - y plane of Cartesian coordinates. The field is symmetric about the z axis, and the coordinate system used employs the cylindrical coordinates z and $R = (x^2 + y^2)^{1/2}$. The plane $z = -z_0$ passes through the center of the foil, and z' is the position of the electron at $t = 0$. We also have simplified the equations by setting the dielectric function of the oxide layer and the spacer to unity.

The potential in Eq. (1), which is due to the motion of an electron in Fourier space in the presence of a thin foil having a dielectric response function $\epsilon_F(\omega)$, is now applied to an oblate spheroidal, metal particulate whose center is at a distance $z_0 - L/2$ above the surface of the thin foil. The applied field induces multipole moments of various strengths in the metal particle. We only consider the induced electric dipole and quadrupole moments. Because of the geometry of the metal particulate, it is best to switch to oblate spheroidal coordinates. We calculate the potential inside and outside the metal particulate and

match boundary conditions at the particulate's surface to find the multipole expansion coefficients of the applied electric field.⁹ We find that these coefficients are

$$E_{lmp} = \frac{iq\sqrt{3}}{av} \delta_{m,0} \delta_{p,1} (2 - \delta_{l,0}) (-1)^{-l} \times (2l+1)^{1/2} \epsilon_F(\omega) I(\omega), \quad (3)$$

where

$$I(\omega) = \int_0^\infty dk \left[k + i\frac{\omega}{v} \right]^{-1} T(k, \omega) \times \exp \left[-k \left[z_0 - \frac{L}{2} \right] \right] j_l(ka); \quad (4)$$

$j_l(x)$ is the spherical Bessel function and a is the focal length of the particulate. The fact that only the coefficients for which $m = 0$ and $p = 1$ are nonzero results from conservation of angular momentum and the symmetry of the potential about the z axis. Because of this situation, only the electric dipole moment p_z and the quadrupole moment Q_{zz} are nonzero (p_x and p_y are both zero). More general cases are intractable. Using oblate spheroidal coordinates, it is found that for a particulate with complex dielectric function $\epsilon_p(\omega)$,

$$p_z = -\frac{a^3}{3} \frac{\eta_0}{Q_{10}(i\eta_0)} \frac{\epsilon_p(\omega) - 1}{\epsilon_p(\omega) - \epsilon_{10}} E_{101} \quad (5)$$

and

$$Q_{zz} = -\frac{2a^4}{3i\sqrt{15}} \frac{1 + 3\eta_0^2}{Q_{20}(i\eta_0)} \frac{\epsilon_p(\omega) - 1}{\epsilon_p(\omega) - \epsilon_{20}} E_{201}, \quad (6)$$

where

$$\epsilon_{lm} = \frac{P_{lm}(i\eta_0) Q'_{lm}(i\eta_0)}{Q_{lm}(i\eta_0) P'_{lm}(i\eta_0)}, \quad (7)$$

with $\eta = \eta_0$ describing the surface of the oblate spheroid and $P_{lm}(i\eta_0)$ and $Q_{lm}(i\eta_0)$ are associated Legendre functions as given in Smythe.¹³

The power radiated from the metal particulate is calculated in the usual manner¹⁴ neglecting multiple scattering of the radiation by other particulates. The energy radiated per unit frequency interval per unit solid angle from an electric dipole is

$$\frac{d^2 P_{\text{dip}}}{d\omega d\Omega} = \frac{c}{8\pi} \left[\frac{\omega}{c} \right]^4 (\sin^2\theta) |p_z|^2, \quad (8)$$

where c is the speed of light ω is the frequency of the emitted radiation at an observation angle θ with respect to the surface normal, and p_z is the electric dipole moment which is given by Eq. (5) for the present case. The energy radiated per unit frequency interval per unit solid angle from an electric quadrupole is

$$\frac{d^2 P_{\text{quad}}}{d\omega d\Omega} = \frac{c}{128\pi} \left[\frac{\omega}{c} \right]^6 (\sin^2\theta)(\cos^2\theta) |Q_{zz}|^2. \quad (9)$$

III. EXPERIMENT

Junctions were fabricated on 1×3 -in.² glass or quartz microscope slides. The slides were washed in warm water with liquid detergent (Micro) and rinsed in deionized water. An ultrasonic bath in methanol for 15 min, followed by blow drying with nitrogen, provided clean substrates for the junctions.

Machined aluminum masks allowed 11 junctions to be made on a slide, each having an area of 4 mm^2 . Electrical connections to the junctions were made through solder pads of chromium (150 nm thick) overlaid with gold (150 nm thick). Copper screw clamps instead of solid solder provided easy and reliable contact to the pads. The bias voltage and current were measured using a four-point probe.

Film deposition took place in a cryopumped, electron-beam evaporator at a pressure of 1×10^{-6} Torr. Film thickness was measured by a quartz crystal monitor positioned near the substrate. The evaporation rate for the lower aluminum electrode was 2 nm/sec. After the film deposition, the bell jar was vented to high-purity oxygen for 15 min. Plasma anodization in a rf discharged¹⁵ increased the oxide to a desirable thickness. A moist oxygen atmosphere at 0.85 Torr with a discharge current of 20 mA for 1 h was sufficient to produce stable light-emitting junctions.

Initially, tunnel junctions were fabricated with aluminum electrodes 80–100 nm thick. Electron micrographs

of these junctions clearly displayed pronounced roughness, as shown in Fig. 1. This texture is also reproduced on the surface of the upper gold electrode. Thinner aluminum electrodes in the (20–30)-nm range reduced this roughness considerably, as shown in Fig. 2. The reduction in roughness is significant and not only produces junctions which may be better quantified but also precludes any untoward high-field dielectric breakdown such as may be enhanced by roughness.

Thus, the thinner [(20–30)-nm-thick] aluminum electrode had the advantage of smooth junction interfaces and better junction stability at high bias voltages. This might be due to an oxide of increased uniformity as well as a reduction of rough protrusions which would serve as high field sites to enhance dielectric breakdown.

Additional micrographs of aluminum on various substrates demonstrated that some small roughness is inherent in the aluminum. Three substrates were tested, polished silicon (Monsanto), quartz slides (Esco Products), and ordinary glass microscope slides (Curtis Matheson). Since all three substrates gave similar results, the inexpensive glass slides were chosen as substrates. The residual roughness did not prove to be nearly as severe a problem for junction stability as the roughness of the (80–100)-nm-thick aluminum.

Gold was deposited to a 10-nm thickness to form the top electrode. A thin insulating layer of magnesium fluoride, 6-nm thick, was then evaporated onto the junction. Silver was deposited on the magnesium fluoride at a

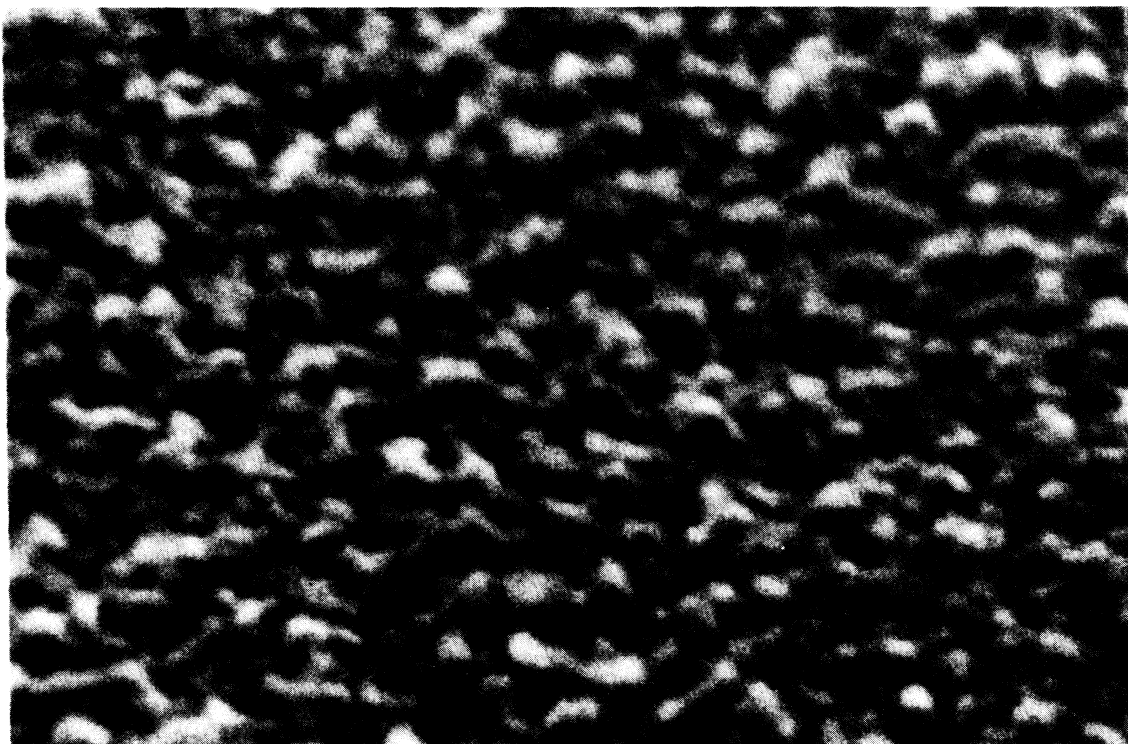


FIG. 1. Electron micrograph of a 100-nm-thick aluminum film on a quartz substrate. Angle of observation is 60° from the substrate normal. (1 cm corresponds to 48 nm.)



FIG. 2. Electron micrograph of a 20-nm-thick aluminum film on quartz. Observation angle is 60° from the normal. Debris in the upper portion of the micrograph is for focusing purposes. (Same magnification as Fig. 1).

rate of 0.2 nm/sec. The silver-island films ranged in mass thickness from 3–9 nm. For all samples, three junctions were covered by a stainless steel plate clamped to the mask during the metal-island evaporation in order to serve as uncoated references. Heating the samples caused the silver islands to bead, forming oblate spheroids. Annealing took place in an open-ended oven at 350°C for 45 sec.

All spectra were obtained with the junction immersed in liquid nitrogen. The efficiency of the detection system as a function of wavelength was measured using a National Bureau of Standards (NBS) tungsten filament lamp. The data presented below were corrected for the efficiency of the system.

IV. RESULTS AND CONCLUSIONS

Figure 3 displays spectra detected along the substrate normal from junctions with various mass thicknesses of the silver-island film. The junctions were dc biased at 3.8 V (aluminum was the negative electrode) and had currents near 27 mA. After emission measurements had been completed, the junctions were viewed in a scanning electron microscope (SEM). The islands formed by annealing a 9-nm-thick silver thin are irregular in shape and clearly not oblate spheroids (Fig. 4). The particulates have major axis lengths ranging from 80–160 nm across. For the 3-nm-thick annealed film, the particulates have a much nar-

rower size and shape distribution and are better modeled as oblate spheroids (Fig. 5). The major axis length is ~ 35 nm, and a minor-to-major axis ratio of 0.4 is reasonable for these spheroids.¹⁰ Tunnel junctions with the 9-nm-thick annealed silver film have a quantum efficiency of $\sim 1 \times 10^{-4}$.

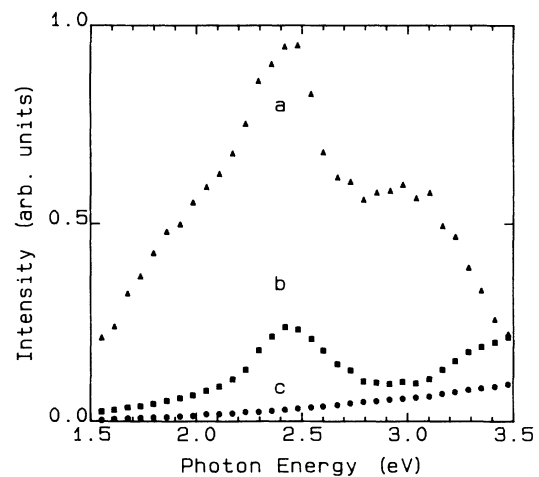


FIG. 3. Spectra from aluminum-alumina-gold tunnel junctions described in the text with annealed silver films of thickness (a) 9 nm, (b) 3 nm, or (c) no silver layer, but annealed.

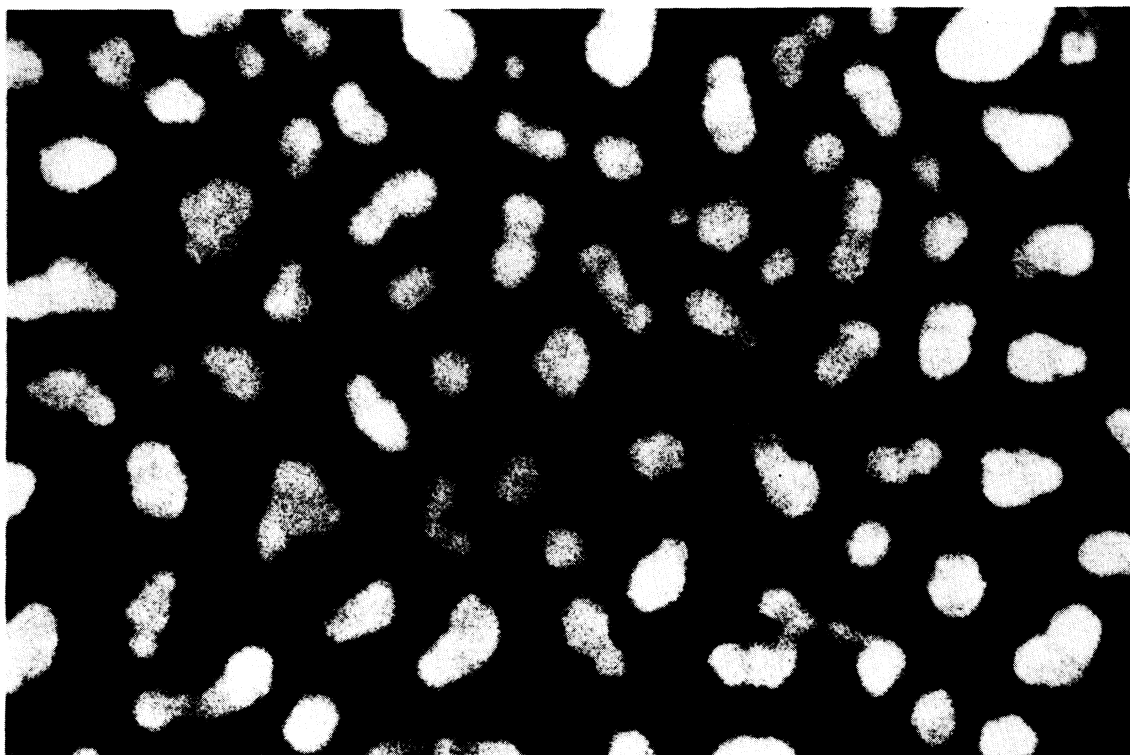


FIG. 4. Electron micrograph of a 9-nm-thick annealed silver film. Observation angle is along the junction normal. (1 cm corresponds to 145 nm.)

For driving fields of wavelengths much longer than the dimensions of the spheroids, only dipole moments are induced in the particulate. Silver oblate spheroids can sustain two dipole modes: one with its dipole moment oriented along the minor axis ($l=1, m=0$) and the other with its dipole moment oriented along the major axis ($l=1, m=1$). The resonant energy of the (1,0) mode is near that of a sphere (i.e., at 3.5 eV) in the nonretarded regime for all minor-to-major axis length ratios, while the (1,1) mode is strongly dependent on shape and is at a lower energy.

Figure 6 shows the calculated total radiated power of the (1,0) mode induced in the silver spheroid by the junction's surface-plasmon driving field using the experimental parameters. The slight discrepancy for experiment and theory may result from errors in the optical data for gold¹⁶ or from other simplifying assumptions made in the calculation.¹⁷ A 15% increase in the real part of the dielectric function of gold would shift the theoretical peak to the observed value. We have also done the same calculation using the experimental parameters of McCarthy and Lambe and have observed that the calculated power peaks near the experimentally observed energy for this case as well.

Figure 7 displays the theoretical power radiated by silver and by gold particulates above a gold foil. For silver particles, there are two peaks for the (1,0) mode. The lower energy peak is strongly driven off resonance and is due to the gold foil, while the second peak occurs

near the resonant energy of the (1,0) mode for isolated silver particulates. Gold particulates display only one peak corresponding to the resonant energy of the (1,0) mode. On the basis of this, a large radiative yield would be expected from gold particulates above a tunnel junction with a gold top electrode. This was tested experimentally, and only a weak, broad peak at 2.4 eV was detected. This is attributed to the strong internal damping of gold at these frequencies compared to silver. In the calculation, the only losses for the induced moments are radiative. The fast surface plasmon modes in the gold foil are subject to internal damping, but a significant portion of the fields associated with these modes lies outside the film and, therefore, the modes are not strongly damped.

For the large particulates of the 9-nm-thick, annealed film, retardation is important, and higher-order modes may be excited.¹⁸ The present calculation does not include retardation or modes higher than the electric dipole and quadrupole moments. Moreover, particulates of this size are not well modeled as oblate spheroids. Our calculations show that as the particulate size increases, the power radiated by the quadrupole mode approaches that of the dipole, and yet it peaks in the vicinity of 2.4 eV. The quadrupole mode is also driven far from its resonant energy by the surface plasmon modes of the gold foil.

Red-shifting the resonant energy of the (1,0) mode in silver should cause the power radiated at 2.4 eV to increase, as the resonance would then lie closer to the driving frequency. Retardation effects red shift the (1,0)

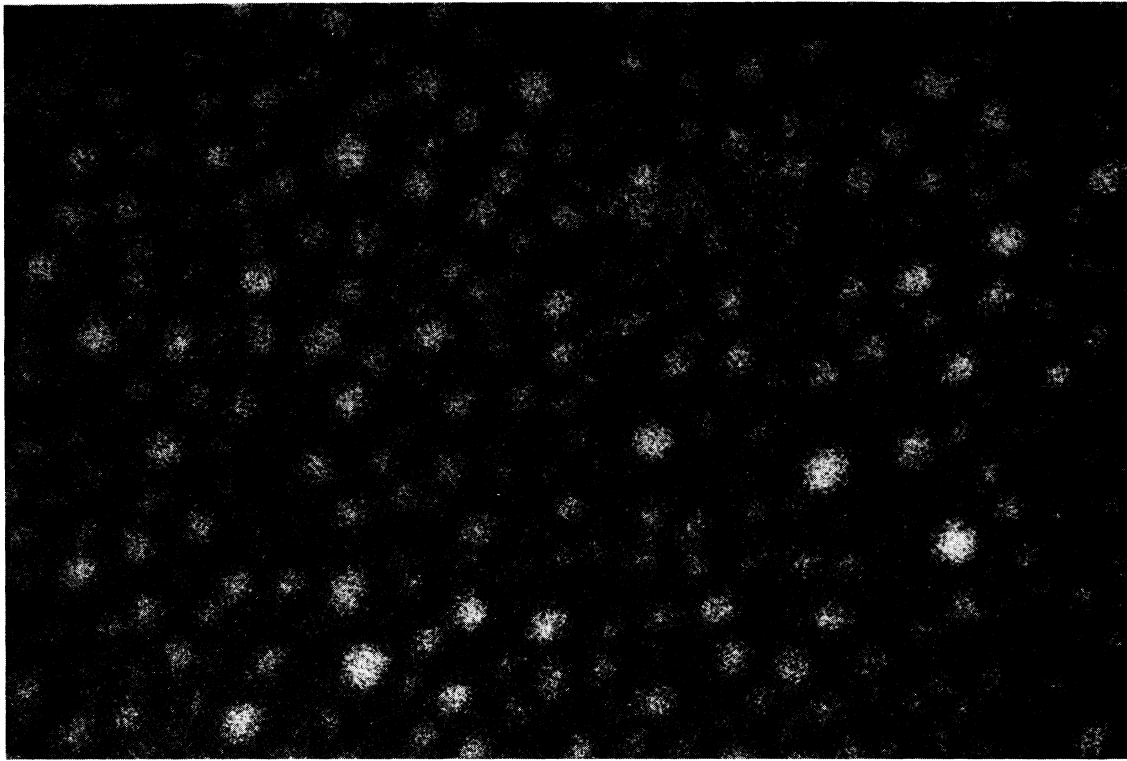


FIG. 5. Electron micrograph of a 3-nm-thick annealed silver film. Observation angle is along the junction normal. (1 cm corresponds to 48 nm.)

mode which would agree with the increased power radiated for thick versus thin annealed silver film. The increase may also be due in part to stimulation of higher-order modes. If a calculation could be accomplished which included retardation effects, then such speculation might be better quantified. Also, a prolate spheroidal model might

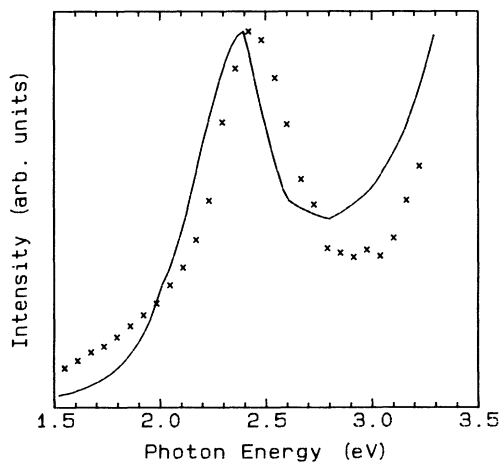


FIG. 6. Solid line: calculation of the power radiated from a 3-nm silver-island film on a 6-nm magnesium fluoride spacer above a 10-nm gold foil. The silver particles were modeled as noninteracting sources, each of which has an oblate spheroidal shape with a major axis length of 35 nm and minor-to-major axis length ratio of 0.4. Dotted line: experiment for the same structure but on an aluminum-alumina layer.

be better suited to the 9-nm film.

Another method of red shifting the mode is to change the shape of the spheroid. The resonant energy of the (1,0) mode decreases as the particulate becomes more spherical. In order to test this, a 6-nm-thick silver film was evaporated on the spacer. A peak near 2.4 eV was detected for this unheated silver film when the junction was biased. The sample was then removed from the liquid nitrogen and annealed in the manner prescribed above. Emission measurements on the annealed sample revealed an increase in the peak height by 15%. No shift in the peak position was observed. The electrical properties were not altered by the annealing, and the slight increase in emission intensity for the sample without silver particulates was subtracted from the peak height. Absorbance measurements in air for a 6-nm, annealed, silver film on quartz showed a red shift in the absorbance peak of 6 nm for the (1,0) mode compared to the unheated film.

Covering the islands with a dielectric medium was also seen to red shift the modes. Absorbance measurements indicated a red shift of 20 nm for the (1,0) mode when overcoating the annealed silver film with 75 nm of magnesium fluoride. Emission spectra from tunnel junctions with the particle layer embedded in magnesium fluoride revealed a decrease in the peak height by 30% compared to the uncoated particulate layer. This is contrary to the above argument, but fields in a dielectric medium are reduced by the square of the index of refraction n . The fields driving the (1,0) modes were reduced in the magnesium fluoride compared to liquid nitrogen by a factor of 22%. The radiative yield is also reduced for spheroids in

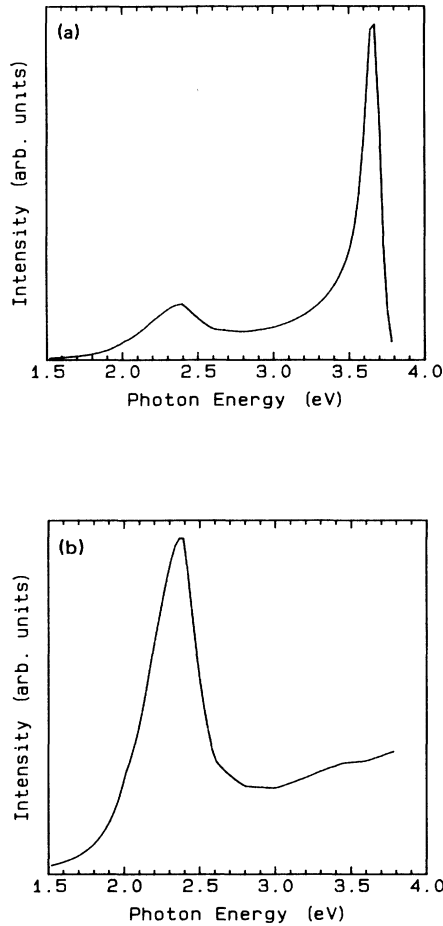


FIG. 7. (a) Calculation of the power radiated from a dipole source in a silver spheroid whose minor-to-major axis length ratio is 0.4 and whose major axis length is 35 nm. The junction bias is 3.8 V. (b) Same calculation, but for gold spheroids.

a dielectric medium by a factor of n^4 .¹¹ This further reduces the yield by another 39%. These losses are partially offset by the red shift of the (1,0) resonance of particulates in magnesium fluoride compared to liquid nitrogen but are in reasonable agreement with our observations.

Figure 8 is the radiation pattern measured near the peak in the spectra for the 9-nm-thick, annealed silver film. The pattern is similar to that of tunnel junctions on rough substrates.¹⁹ For these statistically rough junctions, fast mode surface plasmons associated with the top electrode are scattered by roughness features on the electrode itself. The simple theoretical model developed here furnishes information on peak positions but not on the radiation pattern. The expressions for the radiated power neglect interparticle interactions and the dielectric effect of the multiple thin film system on which the particles reside. The radiation pattern for spheres directly on the aluminum layer can be interpreted to some extent by the simple antenna theory of Refs. 5–7. In their calculations,

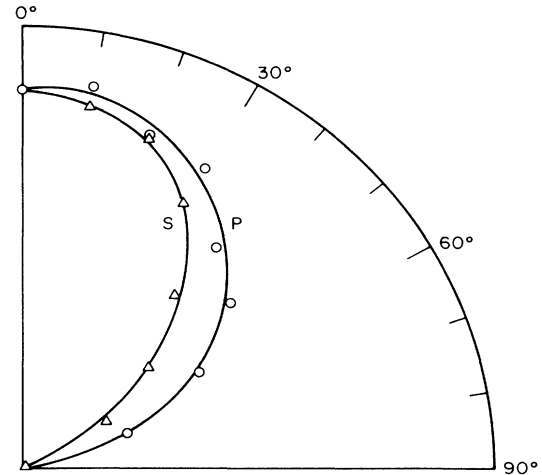


FIG. 8. Radiation pattern for a 9-nm silver-island film on a 6-nm magnesium fluoride spacer (0° lies along the junction normal).

gold spheres are only 3 nm above a semi-infinite aluminum electrode. It is possible that other modes contribute to the radiation, especially for large particles where retardation is important.

The emission of s -polarized light by the junctions is not accounted for in our calculations. However, it may be shown that an electron traveling in the z direction, but along a grazing-incidence trajectory with respect to an oblate spheroid, engenders a strong (1,1) dipole mode.²⁰ This would produce both additional p -polarized and s -polarized light in the theoretical radiation pattern. The only difficulty in comparing the pattern with our experimental results is that the theory would show emission of s -polarized light along the direction tangential to the top electrode as well as other directions. We do not observe this. However, the cross section for scattering and absorption of s -polarized light encountering the large number of particles presented tangentially is large compared to that for p -polarized light. For instance, if the minor-to-major ratio is 0.4, the s -polarization cross section is at least an order of magnitude greater for each particulate than that for p -polarization. Thus, the radiation pattern observed by Little *et al.*,^{10,11} which presented p -polarized light emission tangential to the sample, does not preclude the possibility that s -polarized light would be greatly reduced in the tangential direction by the other particulates encountered by the radiation emitted by any given particulate. However, additional calculations and data would be required to confirm this speculation.

The power emitted from the type of junction used in this paper is weak. The dipole mode along the major axis of the particle has a resonant energy near the peak energy of the driving field of the gold foil. A large increase in radiative yield can be expected if the spheroids are oriented with their major axes along the junction normal.

In summary, we have shown that a crude model of the

driving field and the radiative surface plasmon modes can give the correct spectrum of the photon yield. Also, we have presented data using junctions with controlled parameters showing that further theoretical work is warranted and have speculated as to the analysis needed for explaining the data. By reducing the roughness of the aluminum and using microstructures which can be characterized from optical absorbance measurements, we have obtained data which may permit better agreement between theory and experiment in the future.

ACKNOWLEDGMENTS

We would like to acknowledge support of the Office of Health and Environmental Research and Electric Energy Systems, U.S. Department of Energy (DOE), under Contract No. DE-AC05-84OR21400 with Martin Marietta Energy Systems, Inc.; the Oak Ridge Associated Universities; and the Strategic Defense Initiative Office under DNA Task Code X99QMXXD and Work Unit Code 00003, Air Force Weapons Laboratory, under Interagency Agreement DOE No. 40-1418-83.

-
- ¹S. L. McCarthy and J. Lambe, *Appl. Phys. Lett.* **30**, 427 (1977).
²A. Adams and P. K. Hansma, *Phys. Rev. B* **23**, 3597 (1981).
³A. Adams, J. C. Wyss, and P. K. Hansma, *Phys. Rev. Lett.* **42**, 912 (1979).
⁴P. K. Hansma and H. P. Broida, *Appl. Phys. Lett.* **32**, 545 (1978).
⁵D. Hone, B. Muhlshlegel, and D. J. Scalapino, *Appl. Phys. Lett.* **33**, 203 (1978).
⁶R. W. Rendell, D. J. Scalapino, and B. Muhlshlegel, *Phys. Rev. Lett.* **41**, 1746 (1978).
⁷R. W. Rendell and D. J. Scalapino, *Phys. Rev. B* **24**, 3276 (1981).
⁸R. J. Warmack and S. L. Humphrey, *Phys. Rev. B* **34**, 2246 (1986).
⁹S. W. Kennerly, J. W. Little, R. J. Warwack, and T. L. Ferrell, *Phys. Rev. B* **29**, 2926 (1984).
¹⁰J. W. Little, T. A. Callcott, T. L. Ferrell, and E. T. Arakawa, *Phys. Rev. B* **29**, 1606 (1984).
¹¹J. W. Little, T. L. Ferrell, T. A. Callcott, and E. T. Arakawa, *Phys. Rev. B* **26**, 5953 (1982).
¹²A. Gras-Marti, P. M. Echenique, and R. H. Ritchie, *Surf. Sci.* **173**, 310 (1986).
¹³W. R. Smythe, *Static and Dynamic Electricity* (McGraw-Hill, New York, 1968).
¹⁴J. D. Jackson, *Classical Electrodynamics* (Wiley, New York, 1975).
¹⁵Hummer V, manufactured by Technics, Alexandria, Virginia.
¹⁶H. J. Hageman, W. Gudat, and C. Kunz, Deutsches Elektronen-Synchrotron (Hamburg) Report No. DESY-Sr-74/7, 1974 (unpublished).
¹⁷Further calculations reveal better agreement if the actual values of the dielectric functions of the oxide and spacer are included in the calculation.
¹⁸B. K. Russell, J. G. Mantovani, V. E. Anderson, R. J. Warmack, and T. L. Ferrell, *Phys. Rev. B* **35**, 2151 (1987).
¹⁹P. Dawson, D. G. Walmsley, H. A. Quinn, and A. J. Ferguson, *Phys. Rev. B* **30**, 3164 (1984).
²⁰B. L. Illman, V. E. Anderson, R. J. Warwick, and T. L. Ferrell (unpublished).

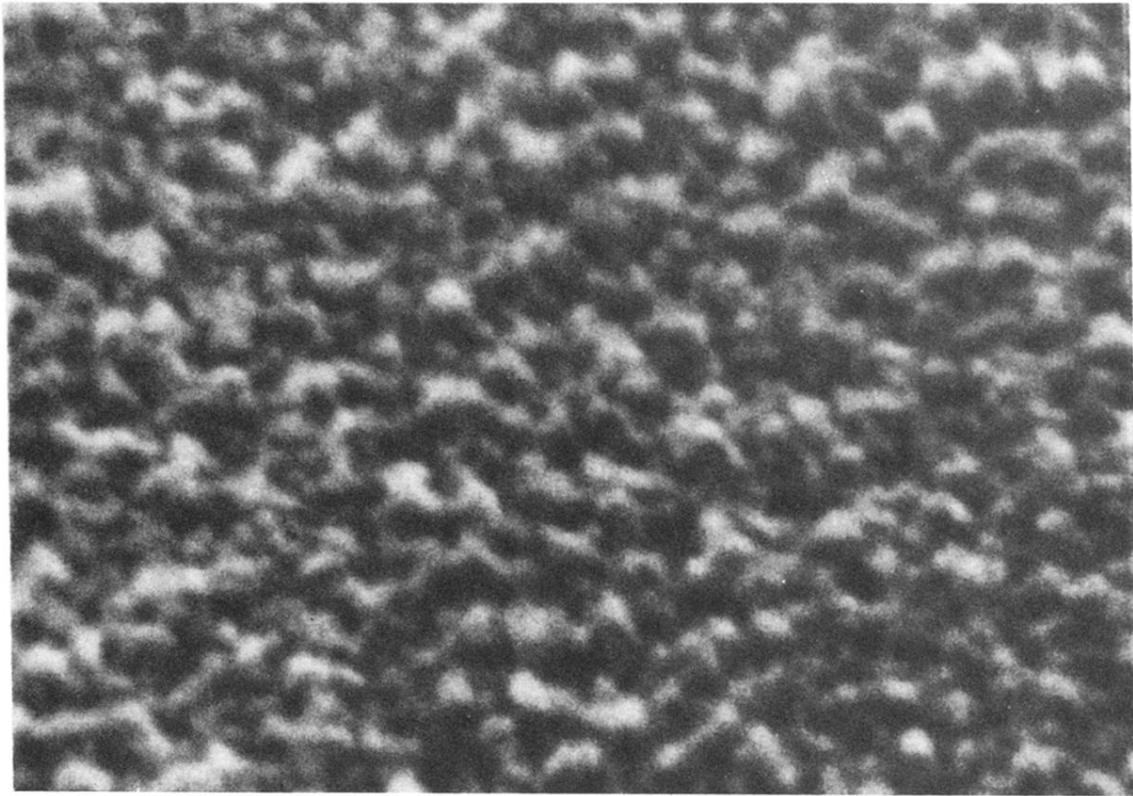


FIG. 1. Electron micrograph of a 100-nm-thick aluminum film on a quartz substrate. Angle of observation is 60° from the substrate normal. (1 cm corresponds to 48 nm.)

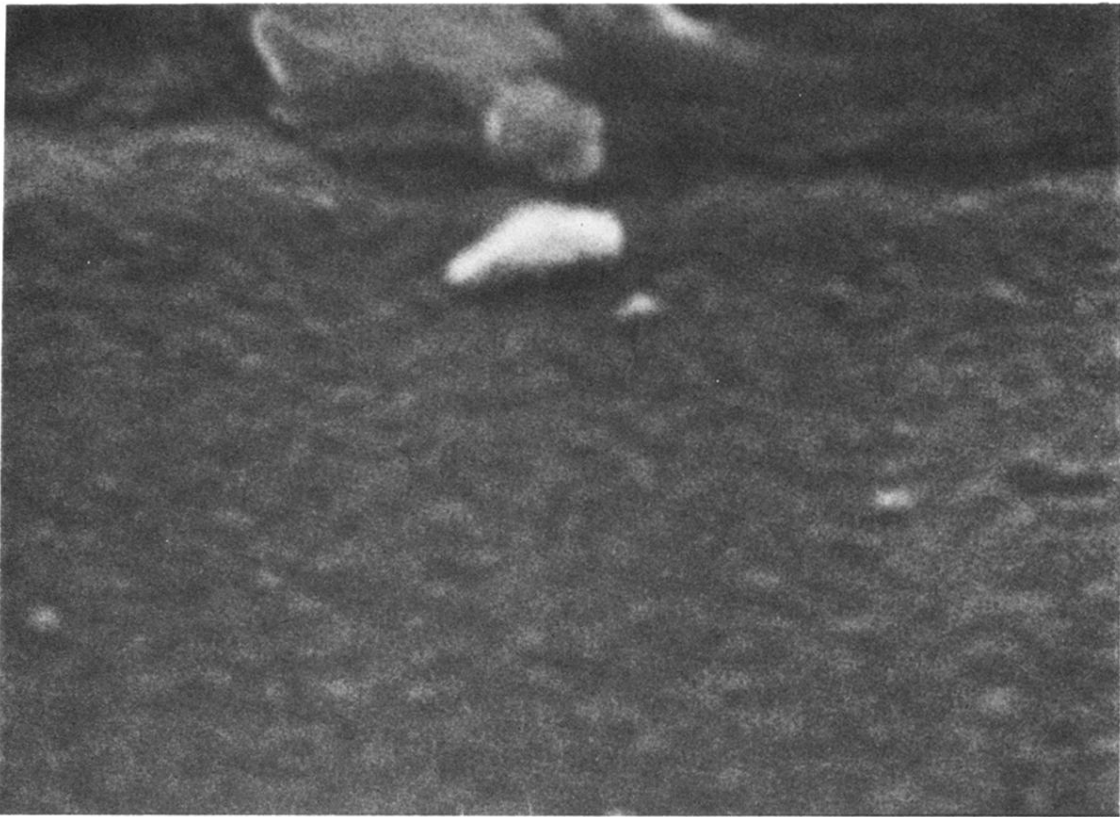


FIG. 2. Electron micrograph of a 20-nm-thick aluminum film on quartz. Observation angle is 60° from the normal. Debris in the upper portion of the micrograph is for focusing purposes. (Same magnification as Fig. 1).

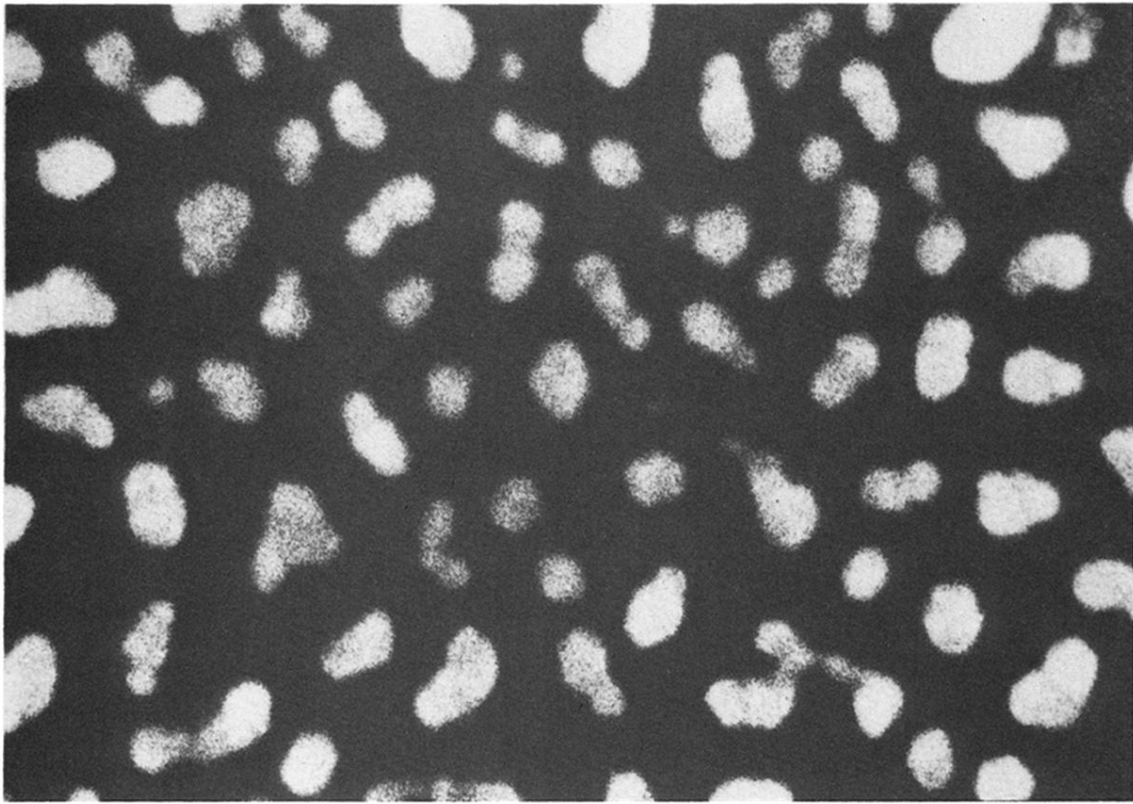


FIG. 4. Electron micrograph of a 9-nm-thick annealed silver film. Observation angle is along the junction normal. (1 cm corresponds to 145 nm.)

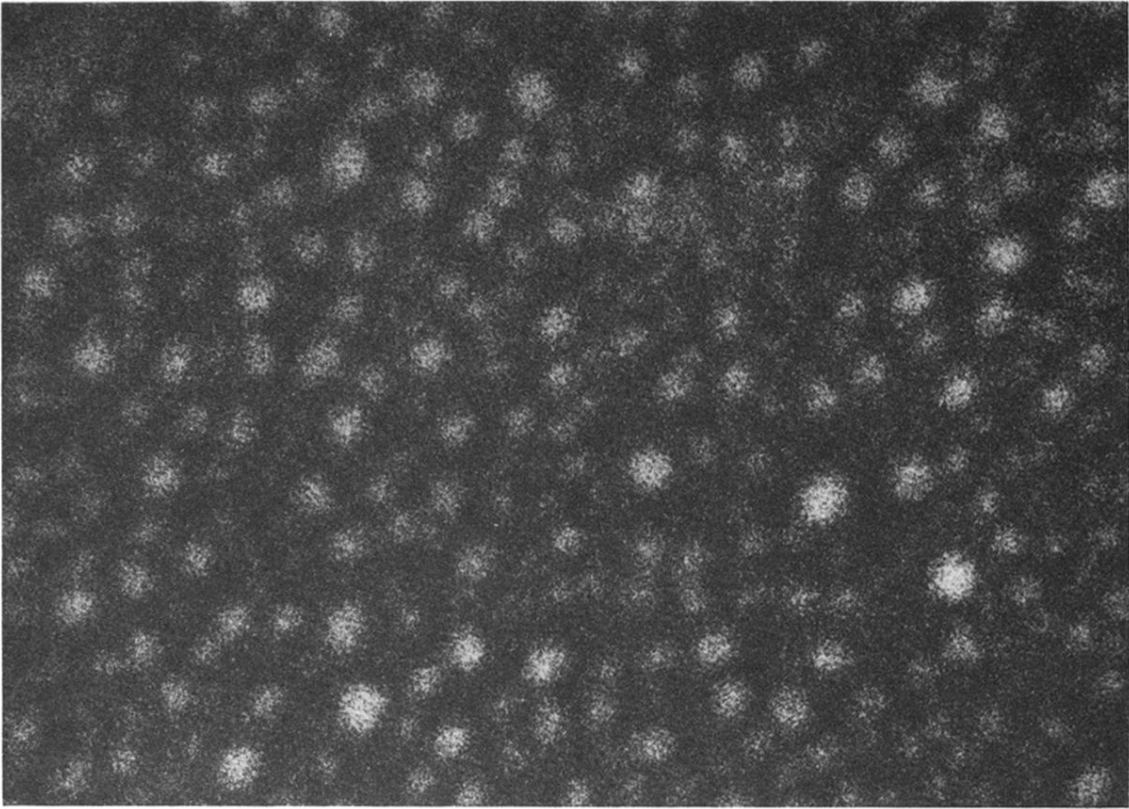


FIG. 5. Electron micrograph of a 3-nm-thick annealed silver film. Observation angle is along the junction normal. (1 cm corresponds to 48 nm.)